Mon. Not. R. Astron. Soc. **331,** 537–544 (2002)

Shocked molecular gas towards the supernova remnant G359.1−0.5 and the Snake

J. S. Lazendic,[1,2★†] M. Wardle,[1] M. G. Burton,[3] F. Yusef-Zadeh,[4] J. B. Whiteoak,[2] A. J. Green[1] and M. C. B. Ashley[3]

[1]*School of Physics A28, University of Sydney, Sydney, NSW 2006, Australia*
[2]*Australia Telescope National Facility, CSIRO, PO Box 76, Epping, NSW 1710, Australia*
[3]*School of Physics, University of New South Wales, Sydney, NSW 2052, Australia*
[4]*Department of Physics and Astronomy, Northwestern University, Dearborn Observatory, 2131 North Sheridan Road, Evanston, IL 60201-2900, USA*

Accepted 2001 November 29. Received 2001 November 29; in original form 2001 June 22

ABSTRACT

We have found a bar of shocked molecular hydrogen (H_2) towards the OH(1720 MHz) maser located at the projected intersection of supernova remnant (SNR) G359.1−0.5 and the non-thermal radio filament known as the Snake. The H_2 bar is well aligned with the SNR shell and almost perpendicular to the Snake. The OH(1720 MHz) maser is located inside the sharp western edge of the H_2 emission, which is consistent with the scenario in which the SNR drives a shock into a molecular cloud at that location. The spectral line profiles of ^{12}CO, HCO^+ and CS towards the maser show broad-line absorption, which is absent in the ^{13}CO spectra and most probably originates from the pre-shock gas. A density gradient is present across the region and is consistent with the passage of the SNR shock, while the H_2 filament is located at the boundary between the pre-shock and post-shock regions.

Key words: masers – shock waves – ISM: clouds – ISM: individual: G359.1−0.5 – ISM: individual: Snake – supernova remnants.

1 INTRODUCTION

OH(1720 MHz) maser emission detected towards supernova remnants (SNRs) has been attributed to shock waves driven into adjacent molecular clouds (Frail, Goss & Slysh 1994). The production of this maser emission, without the simultaneous production of maser emission in the other three ground-state OH transitions at 1612, 1665 and 1667 MHz, requires specific conditions (gas density $n_{H_2} \sim 10^5\,cm^{-3}$, gas temperature $T_{kin} \sim 50-125\,K$, OH column density $N_{OH} \sim 10^{15}-10^{16}\,cm^{-2}$) which can be attained in the cooling gas behind a non-dissociative shock wave (Lockett, Gauthier & Elitzur 1999; Wardle 1999). Surveys by Frail et al. (1996), Green et al. (1997) and Koralesky et al. (1998) have found that about 10 per cent of ∼180 observed Galactic SNRs are associated with OH(1720 MHz) masers. The detection fraction increases to 30 per cent for objects in the Galactic Centre region (Yusef-Zadeh et al. 1996a).

Perhaps the most striking result of the survey towards the Galactic Centre region is the detection of OH masers along the radio continuum shell of the SNR G359.1−0.5 (Yusef-Zadeh, Uchida & Roberts 1995; Yusef-Zadeh et al. 1996b). The brightest of the masers (maser A from Yusef-Zadeh et al. 1995) occurs where a non-thermal filament known as 'the Snake' appears to cross the western edge of the SNR shell. The filament differs from other Galactic Centre non-thermal filaments in showing a number of kinks along its 20-arcmin extent (Gray et al. 1995), and its origin is not well established (Nicholls & Le Strange 1995; Uchida et al. 1996; Benford 1997). The latest model by Bicknell & Li (2001) proposes that the Snake is a magnetic flux tube anchored in dense rotating material. It has been suggested that the Snake is interacting with the shell of G359.1−0.5 because both objects show change in brightness at the apparent crossing point (Uchida, Morris & Yusef-Zadeh 1992; Gray et al. 1995). This could, however, be an artefact resulting from superposition of disparate components along the line of sight. Nevertheless, the presence of an OH(1720 MHz) maser – a signature of SNR/molecular cloud interaction – at this location is quite intriguing. In order to investigate the proposed interaction between the Snake and the SNR, and to characterize the ambient molecular gas in the region, we observed molecular hydrogen (H_2) and a number of other molecular species, particularly searching for signatures of shocked gas. The observations are discussed in Section 2; the results are presented in Section 3 and discussed in Section 4. The conclusions are presented in Section 5.

★Present address: Harvard–Smithsonian Center for Astrophysics, 60 Garden Street, Cambridge, MA 02138, USA.
†E-mail: lazendic@head-cfa.harvard.edu

2 OBSERVATIONS

2.1 UNSWIRF observations

The observations towards maser A [RA(1950) = $17^h41^m46\overset{s}{.}042$, Dec. (1950) = $-29°49'51\overset{''}{.}03$] were carried out in 1998 June with the University of New South Wales Infrared Fabry–Perot (UNSWIRF: Ryder et al. 1998) on the Anglo–Australian Telescope (AAT). Two data sets comprising five and six Fabry–Perot frames, each spaced by 40 km s^{-1}, were taken in the 2.12-μm H_2 1–0 S(1) transition. An additional frame was taken at a setting of −400 km s^{-1} to enable subsequent continuum subtraction. The integration time was 120 s per frame. A resulting image has a diameter of 100 arcsec and a pixel size of 0.77 arcsec. The velocity resolution was ∼75 km s^{-1} FWHM. All the data were reduced using modified routines in the IRAF software package as described in Ryder et al. (1998). Intensity calibration was performed using the standard star BS 5699. A velocity cube was constructed by averaging the frames at the same Fabry–Perot setting from two data sets, and was then fitted with the instrumental Lorentzian profile to determine the line flux (to within 30 per cent) and central velocity (to within 20 km s^{-1}) for the H_2 emission across the field. We note that these data do not provide a true velocity–spatial cube of the emission, as the instrument does not have the velocity resolution to provide an accurate line velocity at each position. Rather, the line velocity is the central velocity at each position. Changes in line centre velocity can, however, be determined. To confirm the detection, the observations were repeated in 1999 June for the 1–0 S(1) line and additional observations were obtained in the 2.25-μm H_2 2–1 S(1) line. On this occasion five Fabry–Perot frames were used for both transitions, with an integration time of 180 s per frame. To establish the coordinate scale for the UNSWIRF images, we used the positions of stellar sources in the *K*-band continuum image listed in the Two Micron All Sky Survey (2MASS) point source catalogue (Cutri 1997) (which has an accuracy of ≈0.1 arcsec).

2.2 SEST observations

A millimetre-line survey towards maser A was carried out with the 15-m SEST at La Silla, Chile, during 2000 June. Position-switching was used with a reference position at RA(1950) = $17^h45^m00^s$, Dec.(1950) = $-31°00'00''$. For periodic pointing calibration and focusing, the 3-mm SiO maser of AH Sco was observed. The main-beam brightness temperature (T_{mb}) scale of the spectra was calibrated on-line using a blackbody calibration source at ambient temperature, and later corrected for the telescope main-beam efficiency (0.74, 0.70, 0.67 and 0.45 at 85–100, 100–115, 130–150 and 220–265 GHz respectively). Simultaneous observation of transitions in two different bands was available using dual SIS receivers at 3 and 2 mm, or 3 and 1.3 mm.

For spectral-line observing we used an acousto-optical spectrometer split into two 43-MHz bands, each with 1000 channels, providing velocity coverages ranging from 60 to 100 km s^{-1} and velocity resolution ranging from 0.06 to 0.14 km s^{-1} across the total wavelength range. A low-resolution spectrometer with resolution of ∼1–2 km s^{-1} was also used simultaneously to determine the spectral baselines in the case of broad-line emission. The final data were smoothed over three channels. The observed transitions, frequencies and antenna beamsizes (FWHM) are listed in Table 1. For the ^{12}CO, ^{13}CO and CS transitions we obtained maps with approximately half-beam and one-beam sampling intervals at lower and higher transitions respectively. The final images covered the 2 × 2 arcmin^2 region around maser A that coincides with the UNSWIRF field of view. The integration time was 30 s for CO isotopomers and 90 s for CS transitions. A set of spectra on-source and at offsets of 20 arcsec in RA and Dec. was obtained for each of the other molecular transitions listed in Table 1, with integration times of 180 s at each position.

Table 1. The first column lists observed molecular species, the next three columns list the SEST observational parameters and the last column gives observed main-beam brightness temperature (T_{mb}) and rms noise towards the maser A.

Molecule	Transition	Frequency (GHz)	Beamsize (arcsec)	T_{mb} (K)
^{13}CO	2–1	220.399	23	0.78 ± 0.21
	1–0	110.201	45	1.20 ± 0.26
^{12}CO	2–1	230.538	23	16.00 ± 0.20
	1–0	115.271	45	10.30 ± 0.50
CS	3–2	146.969	34	0.42 ± 0.12
	2–1	97.981	52	0.54 ± 0.14
HCO^+	1–0	89.188	54	0.48 ± 0.08
$C^{18}O$	2–1	219.560	23	<0.16
	1–0	109.782	45	<0.12
HCN	1–0	88.632	55	<0.17
H_2CO	$3_{(2,2)}$–$2_{(2,1)}$	218.475	24	<0.13
	$3_{(0,3)}$–$2_{(0,2)}$	218.222	24	<0.15
SiO	5–4	217.106	24	<0.14
	2–1	86.848	57	<0.17

The first part of the table lists results from Gaussian fitting of the two ^{13}CO transitions, the line profiles of which peak at −13 km s^{-1} and have linewidths of ∼15–20 km s^{-1}. The second part of the table lists the parameters of ^{12}CO, CS and HCO^+ transitions. Their line profiles suffer broad-line absorption and Gaussian fitting was not possible. We therefore list only the maximum T_{mb} of their line profiles, which occur at −5 km s^{-1}. The third part of the table lists the non-detections. Upper limits are 2σ values.

3 RESULTS AND ANALYSIS

3.1 H_2 emission

Fig. 1 shows contours of velocity-integrated 2.12-μm H_2 1–0 S(1) line emission superimposed on a grey-scale image of the 2MASS *K* band. Some small-scale structures apparent in the H_2 distribution are residuals from subtracting the stellar continuum. A bar of H_2 emission, 1.5 arcmin in length and 15 arcsec in width, extends from the north-east to the south-west. We note, however, that there is weak extensive diffuse emission across the observed region, which was not included in the fitting procedure because of low signal-to-noise ratio. The lowest contour in Fig. 1 thus corresponds to a (4σ) flux level of 2×10^{-5} erg s^{-1} cm^{-2} sr^{-1}. The peak flux density is 10.6×10^{-4} erg s^{-1} cm^{-2} sr^{-1} and the total flux density is 9.2×10^{-13} erg s^{-1} cm^{-2}. After correcting for the typical extinction of the Galactic Centre region (3 mag in *K* band) the parameters of the 1–0 emission are: peak flux density of 1.7×10^{-2} erg s^{-1} cm^{-2} sr^{-1}, total flux density of $(1.4 \pm 0.4) \times 10^{-11}$ erg s^{-1} cm^{-2} and luminosity of ∼33 $L_\odot$. There is no obvious emission in the individual frames of the 2.25-μm H_2 2–1 S(1) data. However, adding the pixels in the central frame of the 2–1 cube over the region delineated by the 1–0 emission, we derive a total flux density of $(2.4 \pm 0.4) \times 10^{-14}$ erg s^{-1} cm^{-2}, which is $\sim 2.9 \times 10^{-13}$ erg s^{-1} cm^{-2} after correcting for extinction. The correspond-

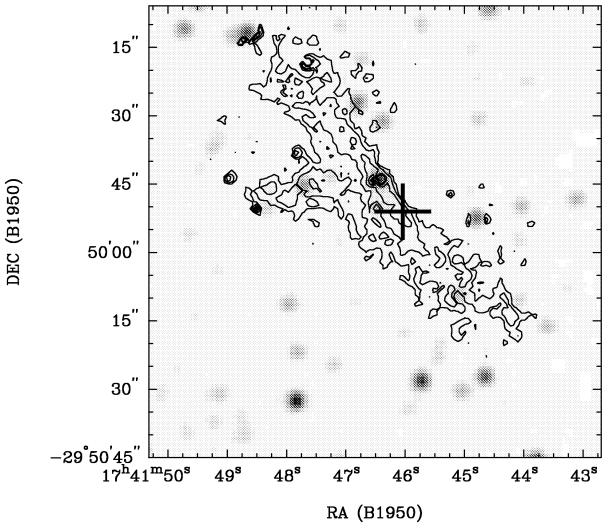

Figure 1. Image of the velocity-integrated 2.12-μm H_2 1−0 S(1) line (contours) overlaid on to the 2MASS *K*-band image (grey-scale). The contours are 13, 20, 30, 45, 56 and 65×10^{-6} erg s^{-1} cm^{-2} sr^{-1}. The cross marks the location of OH(1720 MHz) maser A.

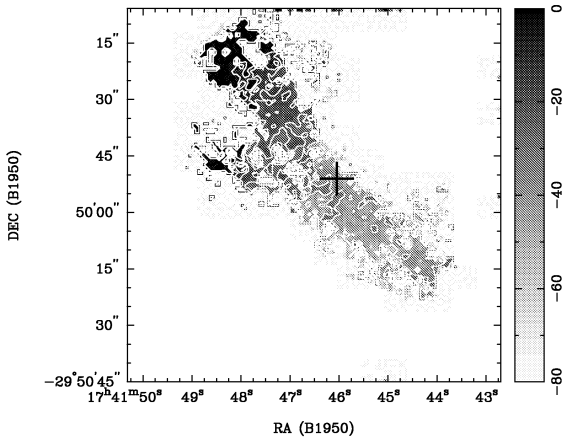

Figure 2. The line centre velocity distribution of the 2.12-μm H_2 1−0 S(1) line emission in both grey-scale and contours. The grey-scale units are km s^{-1} and the contours are −5, −10, −15, −25, −35 and −55 km s^{-1}. The cross marks the location of OH(1720 MHz) maser A.

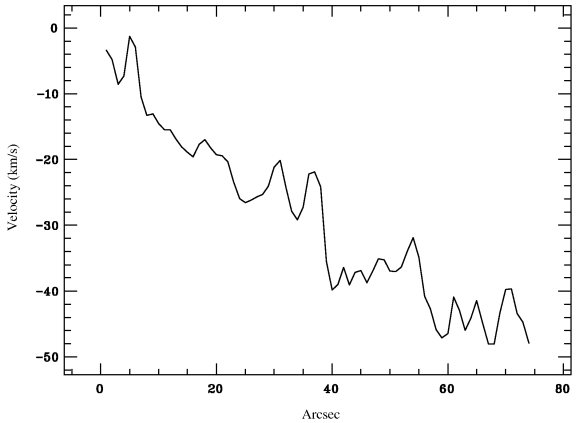

Figure 3. A cut, 5 arcsec wide, along the centre of the H_2 bar extending 80 arcsec diagonally from the top of the bar.

ing total flux density in the 1−0 peak frame is 4.9×10^{-12} erg s^{-1} cm^{-2}. The ratio between the 1−0 and 2−1 line emission is thus ∼20.

The line centre velocity distribution of H_2 1−0 S(1) emission (Fig. 2) shows a systematic velocity gradient along the H_2 bar, with the mean velocity ranging from 0 km s^{-1} in the north to −50 km s^{-1} in the south. These velocities are comparable to the average values of about −13 km s^{-1} for the northern part and −35 km s^{-1} for the southern part obtained from the repeated observations in 2000 June. Fig. 3 shows a cut along the H_2 bar illustrating the velocity gradient. Note that the small-scale structure showing deviations of ∼10−15 km s^{-1} probably reflects the errors in determining the velocity at each position.

The presence of a star [RA(1950) = $17^h41^m46^s.5$, Dec.(1950) = −29°49′45″.0] in the centre of the H_2 filament, together with the velocity difference between the north-eastern and south-western sections, and the jet-like appearance of the brightest H_2 contours, would be consistent with a collimated bipolar jet originating from the star. However, other considerations suggest that this is unlikely. First, the star in question cannot be a protostar. The 2MASS point source catalogue gives the *J*, *H* and *K* magnitudes of the star as 13.22 ± 0.04, 10.31 ± 0.05 and 8.97 ± 0.04 respectively. Using the *JHK* intrinsic colours from Bessell & Brett (1988) and Koornneef (1983), and the reddening vector from Bessell & Brett (1988), we find that the extinction in *K* band is $A_K \approx 2$ (visual extinction $A_V \approx 20$). These values are consistent with the lack of detection in the Digitized Sky Surveys (DSS). After correcting for extinction, we find that the derived magnitudes are consistent with either a K dwarf within 100 pc of the Sun, or a K or M giant at a distance of several kpc. The former case can be excluded given that there are no molecular clouds within 200 pc of the Sun that could give rise to the H_2 emission. In the latter case the bright star is evolved and cannot be driving the outflow. The apparent location of the star at the centre of the H_2 bar is, therefore, most probably a chance alignment. Of course, it is possible that the apparent outflow is being produced by a star at several kpc that is too faint to be detected. A more serious problem is that the emission does not resemble that of other outflows detected in the 1−0 S(1) line. In bipolar outflows, such as Cep E (Eisloffel et al. 1996), the emission associated with jets generally peaks in discrete knots or lobes at some distance from the driving source. Furthermore, the jets are narrow close to the driving source and the lobes have distinct, roughly constant velocities. The velocity gradient and morphology, including the extended diffuse component, present in our H_2 data are thus not consistent with entrainment by a fast, narrow protostellar jet.

Fig. 4 shows contours of velocity-integrated H_2 line emission superimposed on a 6-cm grey-scale VLA image with a resolution of 12.7×8.2 arcsec^2 (PA = 62°) (Yusef-Zadeh et al., in preparation). The bar of H_2 emission is almost perpendicular to the Snake and it runs parallel to the edge of an elliptical depression located ∼15 arcsec to the west of the H_2 bar. The synchrotron emissivity of this depression is reduced by ≲30 per cent and it surrounds the Snake filament where it crosses the shell of G359.1−0.5

3.2 Characteristics of the associated molecular cloud

3.2.1 Identifying the cloud associated with G359.1−0.5

Observations of molecular clouds associated with SNRs are potentially subject to confusion because of other molecular clouds

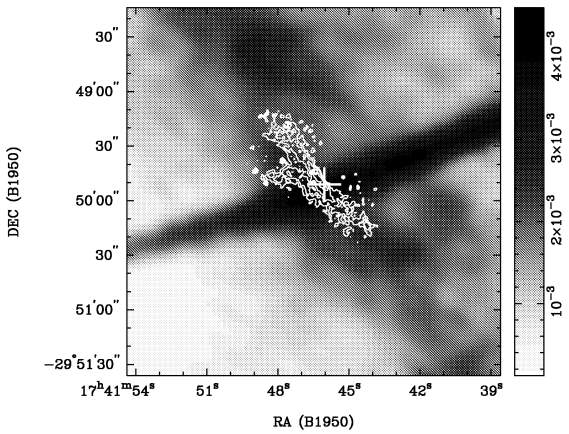

Figure 4. The velocity-integrated image of the H_2 line emission (contours) and the 6-cm radio continuum image (grey-scale). The H_2 filament is located where the Snake (the dark east–west bar) crosses the shell of G359.1−0.5 (dark band extending almost north–south). The grey-scale units are Jy beam^{-1} and the contours are 13, 20, 30, 45, 56 and 65×10^{-6} erg s^{-1} cm^{-2} sr^{-1}. The cross marks the location of OH(1720 MHz) maser A.

along the line of sight. However, the maser velocity of -5 km s^{-1} can be related to the systemic velocity of the post-shock material next to the SNR shell because the OH(1720 MHz) masers are only seen in orientation where they are transverse to the motion of the expanding shock front. Hence they closely match the systemic velocity of the SNR rather than any local intrinsic expansion. We therefore expect that molecular gas with a similar velocity originates from the molecular cloud associated with G359.1−0.5 In Fig. 5 we show the spectra of ^{12}CO, HCO$^+$, ^{13}CO $J = 1-0$ and CS $J = 2-1$ towards maser A. In the velocity range of interest, between -20 and 0 km s^{-1}, the shape of the ^{13}CO line profile differs from those of the other profiles. Inspection of the velocity cubes implies that emission within this range is most likely associated with the SNR shell. In contrast, the emission between -40 and -20 km s^{-1} and the narrow features at $+5$ and $+16$ km s^{-1} appear to be uncorrelated with the SNR shell or the H_2 bar.

Compared with the ^{13}CO spectra, the ^{12}CO and HCO$^+$ spectra, and to a lesser extent the CS spectra, all show an absorption feature between -20 and -5 km s^{-1}. In Table 1 we list the results of a Gaussian fit to the ^{13}CO feature, but for the other species affected by absorption we give only the maximum of the observed line profiles, which thus represent the minimum T_{mb} for these species.

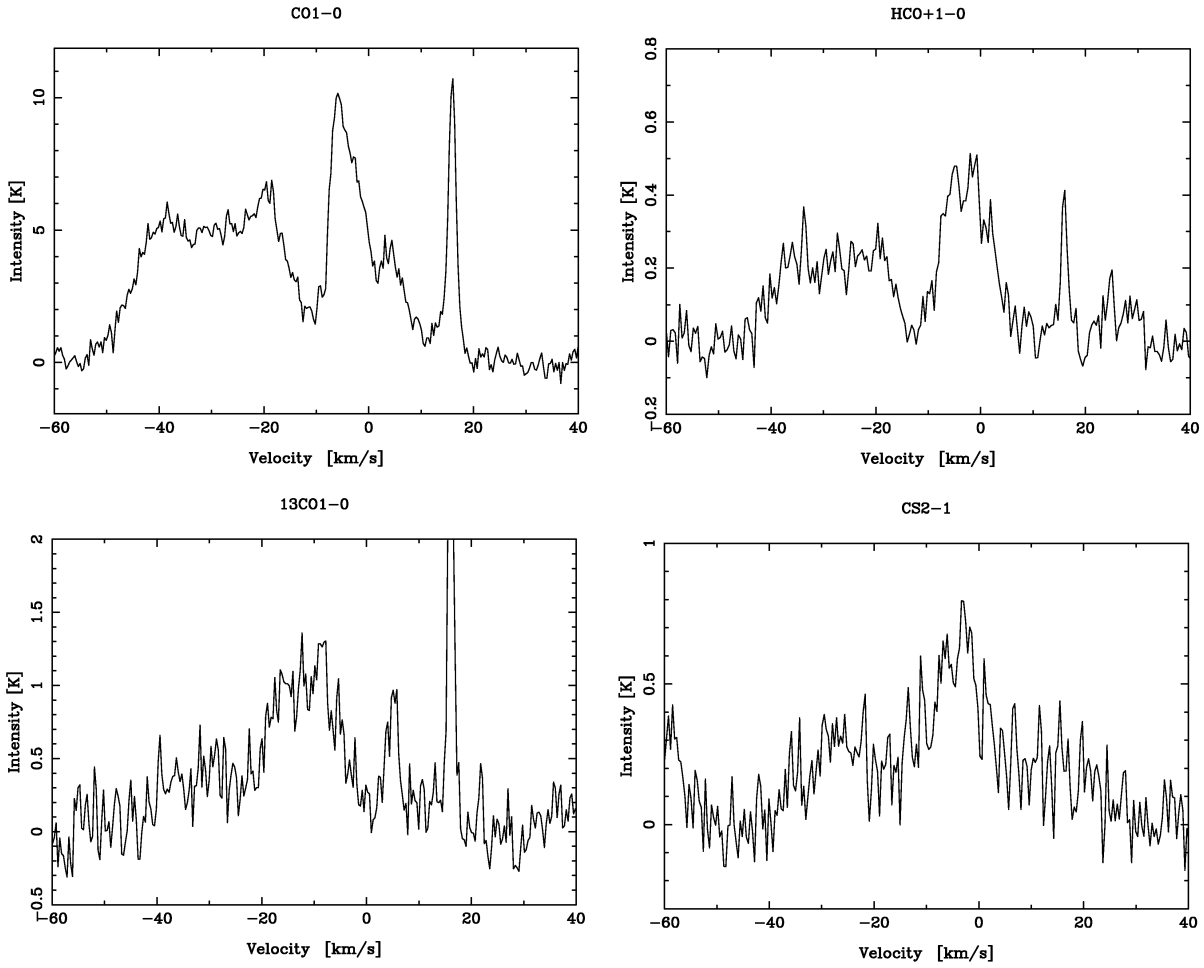

Figure 5. ^{12}CO, HCO$^+$, ^{13}CO $J = 1-0$ and CS $J = 2-1$ spectra towards maser A.

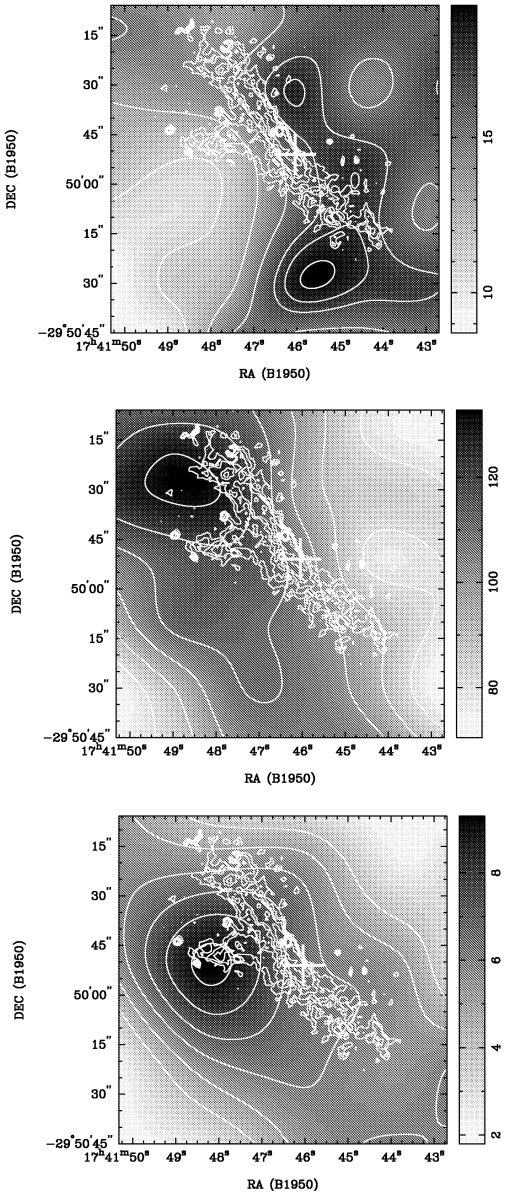

Figure 6. Maps of ^{13}CO $J = 1–0$ (upper), ^{12}CO $J = 1–0$ (middle) and CS $J = 2–1$ (lower) emission (shown in grey-scale with matching contours) integrated between -20 and 0 km s^{-1}, overlaid with the contours of H_2 emission. The H_2 contours are 13, 20, 30, 45, 56 and 65×10^{-6} erg s^{-1} cm^{-2} sr^{-1}. Contour levels (in K km s^{-1}) are (^{13}CO): 9, 11, 13, 15, 17, 18 and 19; (^{12}CO): 70, 80, 90, 100, 110, 120 and 130; (CS): 4, 5, 6, 7, 8 and 9. The cross marks the location of the OH(1720 MHz) maser A.

The correspondence between the peak of the ^{13}CO emission and the centre of the absorption dip in the other three spectra implies that part of the molecular cloud is being self-absorbed in the molecular species with higher optical depth.

The overall distributions of ^{12}CO, ^{13}CO and CS emission show differences caused by variations in optical depth across the region (the spectra of HCO^+ were not obtained over the whole region, as for the other molecules, but only towards the maser and in four positions around the maser). Maps of the emission, integrated between -20 and 0 km s^{-1}, are shown in Fig. 6 overlaid with the contours of H_2 emission. The true distribution of gas column density is represented by the ^{13}CO because of its low optical depth, in contrast to the high optical depths of the other species. We note that the ^{13}CO distribution is dominated by the gas located to the west of the H_2 bar. Although the ^{12}CO- and CS-emitting gas is covering the same region as shown by the ^{13}CO map, these molecules show regions dominated by optically thin gas which is not self-absorbed, and is located east from the H_2 bar. East of the bar we thus have the gas with lower optical depth, while to the west the gas has higher optical depth. The ^{12}CO and CS maps both show an elongated feature near and parallel to the H_2 emission and the SNR shell. The H_2 bar is located at the edge of this filament of molecular gas.

3.2.2 *Physical properties of the molecular cloud*

Self-absorption in molecular clouds can be produced by an overlying colder or sub-thermally excited layer. To estimate the kinetic temperature and density of the gas we have modelled the observed values of the ^{13}CO $J = 2–1$ and $J = 1–0$ line intensities using a statistical equilibrium excitation code supplied by J. H. Black. The code employs a mean escape probability (MEP) approximation for radiative transfer (Jansen, van Dishoeck & Black 1994) and calculates line intensities given the kinetic temperature and density of the gas, the total column density of the molecule and the linewidth. For the western part of the cloud we find a gas temperature of 8 ± 2 K, a gas density of 10^4 cm^{-3}, a ^{13}CO column density of 2.0×10^{16} cm^{-2} and a ^{13}CO $J = 1–0$ optical depth of 0.3. This low optical depth is consistent with the non-detection of C^{18}O transitions. Also, the density of 10^4 cm^{-3} is consistent with the molecular distribution being affected by absorption in this part of the cloud, as the lower excitation temperatures occur at these densities for the HCO^+ and CS lines. Using a ^{12}CO/^{13}CO abundance ratio of 30 (Gardner & Whiteoak 1982) we have a ^{12}CO column density of 6.0×10^{17} cm^{-2} and a ^{12}CO $J = 1–0$ optical depth of 9. On the other hand, the eastern part of the cloud must have a density $\geq 10^5$ cm^{-3} because of the CS $J = 3–2$ detection. For such densities the corresponding gas temperature derived from the code is 10 ± 2 K, the ^{13}CO column is 10^{16} cm^{-2} and the ^{13}CO $J = 1–0$ optical depth is 0.1. This yields a ^{12}CO column density of 3.0×10^{17} cm^{-2} and an optical depth of 3.

These results show that the western region of the cloud may be slightly colder than the eastern region. To investigate whether this difference in temperature is sufficient to produce the observed self-absorption, we use the following:

$$T_{\rm abs} = f(T_{\rm bg})\,{\rm e}^{-\tau_{\rm fg}} + f(T_{\rm fg})(1 - {\rm e}^{-\tau_{\rm fg}}), \quad (1)$$

where

$$f(T) = \frac{h\nu}{k}[({\rm e}^{h\nu/kT} - 1)^{-1} - ({\rm e}^{h\nu/kT_{\rm cmb}} - 1)^{-1}]. \quad (2)$$

$T_{\rm abs}$ is the observed temperature at the velocity of maximum absorption in ^{12}CO, $T_{\rm fg}$ is the excitation temperature of the foreground part of the cloud, $T_{\rm bg}$ is the excitation temperature of the background part of the cloud and $\tau_{\rm fg}$ is the optical depth of the foreground cloud. The observed $T_{\rm abs}$ ranges from 2 to 3.3 K across the mapped region, and $T_{\rm cmb} = 2.7$ K is the temperature of the cosmic microwave background. Using $T_{\rm bg} = 10$ K and $\tau_{\rm fg} = 3$ for the eastern part of the cloud, we derive the foreground cloud excitation temperature of $T_{\rm fg} = 6 \pm 1$ K. For the western part of the cloud $T_{\rm abs}$ depends only on the excitation temperature of the foreground part of the cloud because of the high optical depth in

that region ($\tau_{fg} = 9$). Fitting the observed T_{abs}, we derive the same T_{fg} of 6 ± 1 K.

The kinetic temperature of the western part of the cloud (8 ± 2 K) is in good agreement with the excitation temperature of 6 ± 1 K derived for the foreground part of the cloud. In other words, for the western part of the cloud $T_{kin} = T_{ex}$. Since this is the part of the cloud where ^{12}CO distribution is affected by absorption, we conclude that a physically cold, not sub-thermally excited layer of the cloud is responsible for the self-absorption in the observed spectra.

4 DISCUSSION

The H_2 1–0/2–1 S(1) line ratio of ~20 is consistent with shock excitation, as expected from the presence of the OH(1720 MHz) maser. Although UV excitation can, in principle, produce the 1–0 S(1) line intensity without violating the limit on the 2–1 line when molecular gas of density $10^5 - 10^6$ cm^{-3} is exposed to a far-UV flux of $\gtrsim 10^{4.5} G_0$ (Burton, Hollenbach & Tielens 1990), there is no OB star within 1 pc, as evident from the 2MASS point source catalogue, there are no H II regions apparent in the continuum map, and there is no significant emission in the *Midcourse Space Experiment*[1] (*MSX*) bands at 8.3 and 21.3 μm within an arcminute of the maser.

The H_2 emission must then originate from a shock driven by the SNR. The OH(1720 MHz) maser is expected to be located within the cooling gas behind a C-type shock wave (Lockett et al. 1999), and its location just inside the sharp western edge of the H_2 emission supports the idea that the expanding shell of G359.5–0.1 is driving a shock into a molecular cloud at that location. Shock models *do not* predict the OH column density required to produce OH(1720 MHz) masers (Draine, Roberge & Dalgarno 1983; Kaufman & Neufeld 1996). Lockett et al. (1999) and Wardle (1999) suggested that the OH column density is enhanced by UV photodissociation of H_2O. The internal far-UV field generated by the X-rays from an SNR interior are able to dissociate more than 1 per cent of H_2O, which is enough to produce the required OH abundance (Wardle 1999). How does this far-UV field affects the H_2 emission? It is about 100 times weaker than the standard interstellar field ($G_0 = 1.6 \times 10^{-3}$ erg s^{-1} cm^{-2}), which makes it far less than that associated with an H II region or photodissociation region (PDR). The corresponding local X-ray energy deposition per particle is then $H_x/n \sim 7 \times 10^{-29}$ erg cm^3 s^{-1} [see equation (2) from Maloney, Hollenbach & Tielens (1996)]. From fig. 6(a) in Maloney et al. (1996), the intensity in the 2.12-μm H_2 1–0 S(1) line is 3.2×10^{-5} erg s^{-1} cm^{-2} sr^{-1} which is 0.2 per cent of the observed peak H_2 flux. Thus the far-UV field produced by X-rays makes a negligible contribution to the excitation of the 2.12-μm H_2 1–0 S(1) line.

The H_2 bar follows the distribution of extended OH(1720 MHz) maser emission (Yusef-Zadeh et al. 1995), which is believed to be evidence of this interaction on a global scale (Yusef-Zadeh et al. 1999). Indeed, X-ray observations (Bamba et al. 2000) show a centre-filled morphology of this SNR which, in conjunction with the shell morphology in the radio band, has been proposed as a characteristic of SNRs interacting with molecular clouds (Rho & Petre 1998). We found the H_2 emission near other masers in this SNR to be aligned well with the SNR shell (Lazendic et al., in preparation). The magnetic field along the line of sight towards maser A was estimated to be ~560 μG and the magnetic field was found to be oriented along the H_2 bar (Yusef-Zadeh, Roberts & Bower 2001). The thickness of the shock is expected to be of order 10^{17} cm, about an arcsecond at a distance of 8.5 kpc. We identify the sharp western edge of the bar as being the leading, limb-brightened edge of a curved shock front. The maser velocity is distinct from the mean velocity of about -30 km s^{-1} of the shocked H_2 at this location, but the maser is preferentially produced when the shock front is perpendicular to the line of sight. The H_2 velocity gradient could be the result of a pre-existing gradient, since a gradient of ~5 km s^{-1} is found in the ^{13}CO gas in the same direction.

The results derived from the molecular spectra imply the presence of a density gradient across the region, and the obvious mechanism to produce such a gradient is the passage of an SNR shock wave. The denser gas ($\sim 10^5 - 10^6$ cm^{-3}) then corresponds to post-shock gas and the lower density gas ($\sim 10^4$ cm^{-3}) corresponds to ambient pre-shock gas, with the H_2 filament being the boundary between the two regions. A similar case of self-absorption by pre-shock gas was also seen in IC 443 (White et al. 1987; van Dishoeck, Jansen & Phillips 1993). The values obtained for gas densities are consistent with those expected in shocks. Because of the presence of the OH(1720 MHz) maser, which requires a density $\sim 10^5$ cm^{-3}, the pre-shock density must be $\sim 10^4$ cm^{-3} since the typical compression in shocks is ~ 20–30 (for a shock speed of 20–30 km s^{-1} and an Alfvén speed in molecular clouds of 2 km s^{-1}). In Fig. 7 we present a schematic model of the SNR shock passing through the molecular cloud. Dense gas is located mostly on the eastern side of the H_2 filament, i.e. behind the shock front, while the lower density gas extends mostly to the west from the H_2 emission, i.e. in front of the shock front.

The gas temperature between the pre-shock and post-shock gas does not differ much since the gas cools rapidly behind the C-type shock. We did not detect the warm molecular gas, other than in H_2, found in other SNRs associated with OH(1720 MHz) masers (van Dishoeck et al. 1993; Frail & Mitchell 1998; Reach & Rho 1999). The reason is probably beam dilution. The warm gas is less than 0.6 pc away from the shock front, as inferred from the H_2 emission, and our beam of 1–2 pc in size includes the volume of gas further away that has been cooled to near-ambient gas temperature. The post-shock/ambient cloud temperature of 10 K is consistent with the excitation temperature derived for the clouds in the Galactic Centre region (Oka et al. 1998). The beam dilution might be also the reason for non-detection of H_2CO and SiO transitions which favour regions with higher temperatures. Although the pre-shock gas temperature of ~8 K is lower than typical molecular cloud temperatures of ≥10 K (Goldsmith 1987), dark clouds are found with temperatures low as this (Dickman 1975; Snell 1981). In our case, a likely explanation for this is the broad linewidth of the cloud (15–20 km s^{-1}) which enables more efficient cooling. This is supported by the results of the MEP code. As CO is the dominant coolant at densities $\sim 10^4$ cm^{-3} (Goldsmith & Langer 1978), we can estimate the total cooling rate using the total power in the rotational transition of ^{12}CO. For a ^{12}CO column density of 10^{18} cm^{-2} and volume density of 10^4 cm^{-3}, the power emitted for $\Delta v = 20$ km s^{-1} and $T_{kin} = 8$ K is $\sim 4 \times 10^{-23}$ erg s^{-1} CO^{-1}, and for $\Delta v = 2$ km s^{-1} and $T_{kin} = 15$ K is $\sim 4.7 \times 10^{-23}$ erg s^{-1} CO^{-1}. Thus the cooling rate from an 8-K cloud with 20 km s^{-1} linewidth is similar to that of a 15-K cloud with 2 km s^{-1} linewidth.

Despite the positional coincidence and spatial proximity of the two, we did not find any morphological evidence in our data that

[1] http://www.ipac.caltech.edu/ipac/msx/msx.html

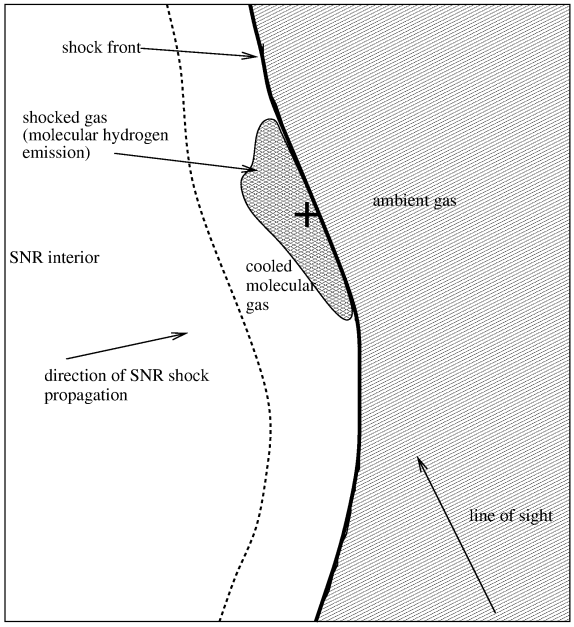

Figure 7. A schematic model of the molecular cloud towards maser A (marked with a cross) is presented to illustrate the distribution of different components. The H_2 bar is located just behind the thin shock front, which is expanding in a direction transverse to the line of sight.

supports the interaction between the SNR and the Snake. Similarly, besides the positional coincidence, there is no obvious relationship between the H_2 emission and the Snake. In the view of the recent suggestion by Bicknell & Li (2001) that the origin of the Snake is linked to rotating molecular clouds, we examined the possibility that the velocity gradient in H_2 of $\pm 20\,\mathrm{km\,s^{-1}}$ might originate from rotation of a flattened cloud. The 1−0 S(1) emission runs along an elliptical depression in the 6-cm emission from the SNR where the Snake crosses it (see Fig. 4). This depression could be caused by a rotating dense molecular cloud. However, we derive the mass of the cloud from our ^{13}CO data to be $\sim 700\,M_\odot$, in which case its escape speed is about $1.6\,\mathrm{km\,s^{-1}}$ and its self-gravity could not sustain the rotation.

5 CONCLUSIONS

We have carried out near-IR and millimetre wavelength observations of the region around the OH(1720 MHz) maser located at the apparent intersection of the non-thermal filament the Snake and the SNR shell G359.1−0.5. A bar of H_2 emission is found encompassing the OH(1720 MHz) maser and aligned with the SNR shell. We suggest that H_2 emission originates from the expansion of the SNR blast wave, which is evident from the sharp western edge that corresponds to the forward shock. This shocked H_2 emission, as inferred from the 1−0 and 2−1 S(1) line ratio, supports the notion that the OH(1720 MHz) masers associated with SNRs are produced in molecular shock waves.

Emission from the molecular species ^{12}CO, CS, HCO^+ and ^{13}CO is detected at the maser velocity. The spectra of the former three species are affected by broad-line absorption which originates from a colder layer of molecular gas. Optically thin ^{13}CO is unaffected by the absorption and is produced mostly in this colder layer, identified as pre-shock gas. The inferred density gradient across the region places higher density post-shock gas west of the H_2 bar. The distribution of the pre-shock and post-shock gas is consistent with the passage of the SNR shock and the H_2 bar being the boundary between the two regions.

The warm molecular post-shock gas is not detected at millimetre wavelengths probably because of beam dilution. For a better morphological and qualitative study of the shocked molecular gas towards maser A, we plan to obtain observations at submillimetre wavelengths, which will have improved spatial resolution. Observations at other maser positions in the SNR are in progress to obtain a global view of the interaction of the SNR G359.1−0.5 with its molecular gas environment.

ACKNOWLEDGMENTS

We thank both the SEST and the AAT for the allocation of observing time. We thank J. Black for use of his MEP code, and M. Cohen, M. Reid and T. Bourke for useful discussions. JSL was supported by the Australian Government International Postgraduate Research Scholarship and the Sydney University Postgraduate Scholarship, and acknowledges travel support from the Access to Major Research Facilities Program of the Australian Nuclear Science & Technology Organization. MW was supported by the Australian Research Council. This publication makes use of data products from: (1) the Two Micron All Sky Survey (2MASS), which is a joint project of the University of Massachusetts and the Infrared Processing and Analysis Center/California Institute of Technology, funded by the National Aeronautics and Space Administration and the National Science Foundation; and (2) the Digitized Sky Surveys (DSS), which were produced at the Space Telescope Science Institute under US Government grant NAG W-2166. The images of these surveys are based on photographic data obtained using the Oschin Schmidt Telescope on Palomar Mountain and the UK Schmidt Telescope. The plates were processed into the present compressed digital form with the permission of these institutions. The National Geographic Society−Palomar Observatory Sky Atlas (POSS-I) was made by the California Institute of Technology with grants from the National Geographic Society. The Swedish−ESO Submillimetre Telescope (SEST) is operated by the Swedish National Facility for Radio Astronomy, Onsala Space Observatory, and by the European Southern Observatory (ESO).

REFERENCES

Bamba A., Yokogawa J., Sakano M., Koyama K., 2000, PASJ, 52, 259
Benford G., 1997, MNRAS, 285, 573
Bessell M. S., Brett J. M., 1988, PASP, 100, 1134
Bicknell G. V., Li J., 2001, ApJ, 548, L69
Burton M. G., Hollenbach D. J., Tielens A. G. G. M., 1990, ApJ, 365, 620
Cutri R. M., 1997, in Garzón F. et al., eds, Astrophys. Space Sci. Library, Vol. 210, The Impact of Large Scale Near-IR Sky Surveys. Kluwer, Dordrecht, p. 187
Dickman R. L., 1975, ApJ, 202, 50
Draine B. T., Roberge W. G., Dalgarno A., 1983, ApJ, 264, 485
Eisloffel J., Smith M. D., Davis C. J., Ray T. P., 1996, AJ, 112, 2086
Frail D. A., Mitchell G. F., 1998, ApJ, 508, 690
Frail D. A., Goss W. M., Slysh V. I., 1994, ApJ, 424, L111
Frail D. A., Goss W. M., Reynoso E. M., Giacani E. B., Green A. J., Otrupcek R., 1996, AJ, 111, 1651
Gardner F. F., Whiteoak J. B., 1982, MNRAS, 199, 23
Goldsmith P. F., 1987, in Hollenbach D. J., Thronson H. A., eds, Astrophys. Space Sci. Library, Vol. 134, Interstellar Processes. Reidel, Dordrecht, p. 51

Goldsmith P. F., Langer W. D., 1978, ApJ, 222, 881
Gray A. D., Nicholls J., Ekers R. D., Cram L. E., 1995, ApJ, 448, 164
Green A. J., Frail D. A., Goss W. M., Otrupcek R., 1997, AJ, 114, 2058
Jansen D. J., van Dishoeck E. F., Black J. H., 1994, A&A, 282, 605
Kaufman M. J., Neufeld D. A., 1996, ApJ, 456, 611
Koornneef J., 1983, A&A, 128, 84
Koralesky B., Frail D. A., Goss W. M., Claussen M. J., Green A. J., 1998, AJ, 116, 1323
Lockett P., Gauthier E., Elitzur M., 1999, ApJ, 511, 235
Loren R. B., Wootten A., 1980, ApJ, 242, 568
Maloney P. R., Hollenbach D. J., Tielens A. G. G. M., 1996, ApJ, 466, 561
Nicholls J., Le Strange E. T., 1995, ApJ, 443, 638
Oka T., Hasegawa T., Sato F., Tsuboi M., Miyazaki A., 1998, ApJS, 118, 455
Reach W. T., Rho J., 1999, ApJ, 511, 836
Rho J., Petre R., 1998, ApJ, 503, L167
Ryder S. D., Sun Y.-S., Ashley M. C. B., Burton M. G., Allen L. E., Storey J. W. V., 1998, Publ. Astron. Soc. Aust., 15, 228
Snell R. L., 1981, ApJS, 45, 121
Uchida K., Morris M., Yusef-Zadeh F., 1992, AJ, 104, 1533
Uchida K. I., Morris M., Serabyn E., Guesten R., 1996, ApJ, 462, 768
van Dishoeck E. F., Jansen D. J., Phillips T. G., 1993, A&A, 279, 541
Wardle M., 1999, ApJ, 525, L101
White G. J., Rainey R., Hayashi S. S., Kaifu N., 1987, A&A, 173, 337
Yusef-Zadeh F., Uchida K. I., Roberts D., 1995, Sci, 270, 1801
Yusef-Zadeh F., Roberts D. A., Goss W. M., Frail D. A., Green A. J., 1996a, ApJ, 466, L25
Yusef-Zadeh F., Robinson B. T., Roberts D. A., Goss W. M., Frail D. A., Green A., 1996b, in Gredel R., ed., ASP Conf. Ser. Vol. 102, The Galactic Center. Astron. Soc. Pac., San Francisco, p. 151
Yusef-Zadeh F., Goss W. M., Roberts D. A., Robinson B., Frail D. A., 1999, ApJ, 527, 172
Yusef-Zadeh F., Roberts D., Bower G., Wardle M., 2001, in Migenes V., ed., IAU Symp. 206, Cosmic Masers: From Protostars to Black Holes. Astron. Soc. Pac., San Francisco, in press

This paper has been typeset from a TEX/LATEX file prepared by the author.